# *Supporting Information*

**Polypyrrole Hydrogel as Universal Precursors for the Target Preparation of Heteroatoms-doped Hierarchical Carbon with atomically distributed metal sites towards High-efficiency ORR and Zn-air Battery**

Wenxue Guo,[a†] Xiaotong Teng,[a,b†] Qinhui Zhao,[a†] Bin Zhang,[a†] Qi Yue,[a] Wei Tan,[b*] Hongmei Du,[c*] Jie Yu,[a*] Baolong Zhou[a*]

[a.] *School of Pharmacy, Weifang Medical University, Weifang, 261053, Shandong, P. R. China*

[b.] *Department of Respiration, The First Affiliated Hospital of Weifang Medical University (Weifang People's Hospital), Weifang, 261000, Shandong, PR China.*

[c.] *School of Basic Medicine, Weifang Medical University, Weifang, 261053, Shandong, PR China.*

[†]These authors contribute equal to this article.

*E-mail: zhoubaolong@wfmc.edu.cn*

[†]These authors contribute equal to this article.

*E-mail: zhoubaolong@wfmc.edu.cn*

**Contents**

## Section 1. Experimental Section

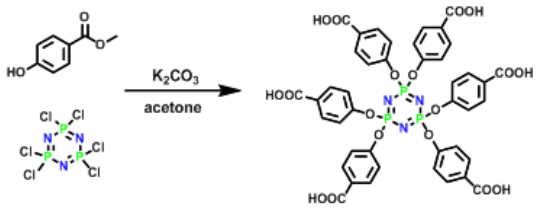


**Scheme 1**. Route for the synthesis of CP

**Preparation of CP**: In a round-bottom flask equipped with a condenser for refluxing and a magnetic stirring bar, methyl 4-hydroxybenzoate (5.78 g, 37.99 mmol), phosphonitrilic chloride trimer (2.00 g, 5.75mmol), potassium carbonate (5.25 g, 37.99 mmol) and dry acetone (100 mL) were added. The mixture was stirred under reflux under argon atmosphere for 24 h, and then cooled to room temperature. After the solvent was removed by rotation evaporation, water (100 mL) and dichloromethane (200 mL) were added. The organic phase was separated and the aqueous phase was extracted with dichloromethane. The organic phase was combined, washed with brine, dried over anhydrous $MgSO_4$, and filtered. After removal of the volatile solvent, the residue was purified by silica gel column chromatography (100~200 mesh) using petroleum ether and ethyl acetate (3:1, v/v) as eluents to afford the hexamethyl intermediate as a pure white solid in 92% yield

To the hexamethyl intermediate (5.50 g, 5.28 mmol) in methanol (25 mL) and THF (25 mL) was added NaOH aqueous solution (4 M, 25 mL). The mixture was stirred under an argon atmosphere at room temperature for 48 h. After the solvent was evaporated, the residue was dissolved in water and acidified with concentrated HCl in an ice-water bath (pH=1~2). The resulting precipitate was collected by suction, washed with water twice, and dried at 70 $^{o}$C under vacuum, affording the target compound as an off-white solid in 97% yield (4.89 g, 5.11 mmol).

**Preparation of CPP-X:** First, the polypyrrole-based hydrogel (PPH) was synthesized using a template-free gelation process through thepolymerization of pyrrole monomers in the presence of CP and $FeCl_3$. Typically, 400 μL pyrrole monomer was added into 3 mL CP solution (0.5 mM in ethanol/water, v/v=1:1). 2.24 g of $FeCl_3$ was dissolved into another 3 mL

CP solution (0.5 mM in ethanol/water, v/v=1:1). After cooling down to about 4 °C, both solutions were mixed together quickly, then aged for 24 h. During polymerization, a crosslinked polymer framework was formed through electrostatic interaction and/or hydrogen bonding between the positively charged groups containing PPH chains and CP, as well as through the chelation effect of iron ions on PPH chains. Thus, a stable black gel was obtained. The obtained PPH was purified with deionized (DI) water and freeze-dried, and then pyrolyzed in argon atmosphere at a heating rate of 5 °C $min^{-1}$ at different temperatures (800, 900, 1000 °C) for 2 hours. The obtained samples were named CPP-800, CPP-900 and CPP-1000, respectively.

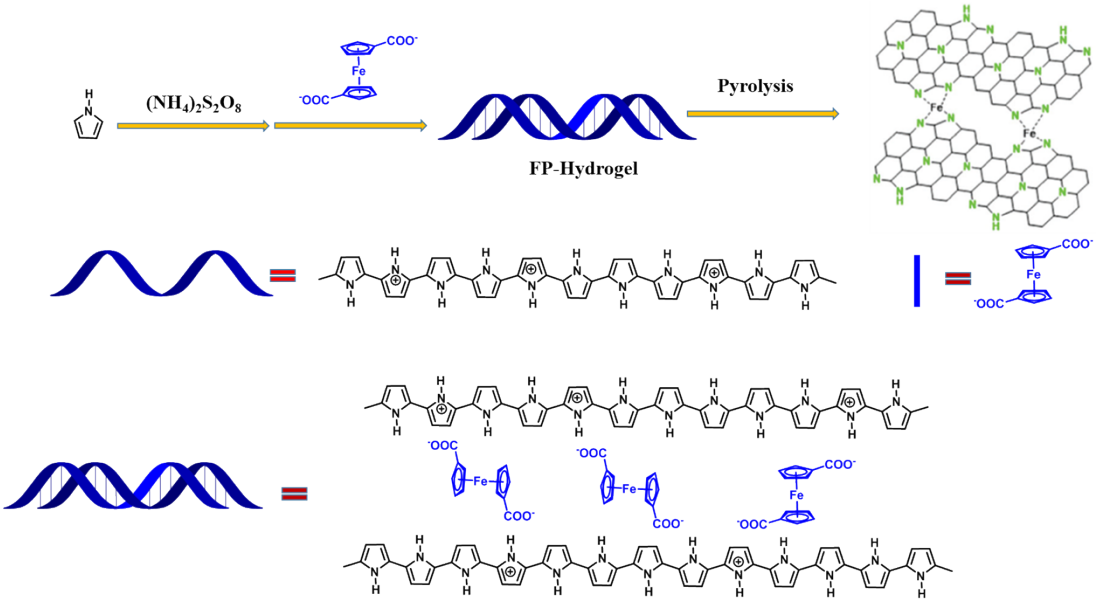


**Scheme 2**. Route for the synthesis of Ferrocene derived single-atom catalysts.

**Preparation of PF-X:** PF-800 was prepared according to our previous work. Briefly, 4.2 mL pyrrole was initially dissolved in 50 mL isopropanol. Then, 1,1'-Ferrocenedicarboxylic acid (1.053 g, 1.1 mmol), NaOH (0.27 g, 6.75 mmol) and ammonium persulfate (13.7 g, 61 mmol) that pre-dissolved in 100 mL $H_2O$ were quickly mixed with pyrrole at the temperature of 4 °C to give the FP hydrogel. The hydrogel was washed by ethanol and water thoroughly, and then subjected to freeze-drying to afford the PF-xerogels. PF-X was prepared via direct carbonization of PF-xreogel directly under the Ar. After finely grinding, PF-xreogel was loaded on a porcelain boat and then transferred into a tube furnace. Then, the pyrolysis was conducted under the atmosphere of Ar and heated to the target temperature (X =700, 800 and

900 °C) for 2 h. The target product, namely PF-X, is obtained after natural cooling to room temperature.

**Preparation of BSMP-800**

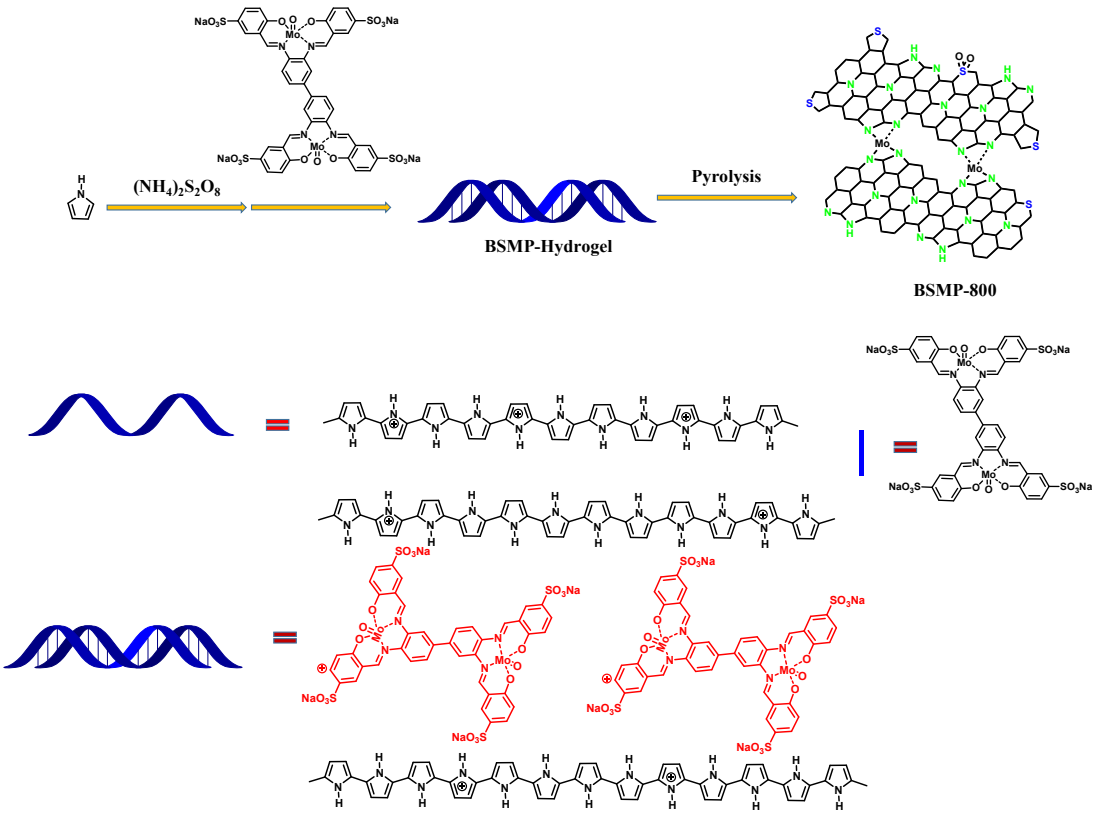


**Scheme 3**. Route for the synthesis of bisalphen derived single-atom catalyst.

The bisalphen *(N,N',N'',N'''*-tetrabis-(salicylidene)-3,30,4,40-biphenylenetetraimino) ligand was prepared as previously described in the literature. The bisalphen ligand (1.58 mmol) was dissolved in ethanol (50 mL) and slowly added dropwise over a suspension of $MoO_2(acac)_2$. The mixture was stirred under nitrogen atmosphere at 80 °C for 24 hours. The solution was refluxed for 36 hours, and the red precipitate was filtered and recrystallized from methanol. The obtained product was stored under vacuum at room temperature. BSMP hydrogel was prepared under the same procedure as the FP-gel. And the final catalysts was obtained via direct carbonization of BSMP at 800 °C.

**Materials Characterization:** The morphologies of powder samples were evaluated by the scan electron microscopy (SEM, Caisi Sigma 300) and the transmission electron microscopy (TEM, JEOL JEM2100PLUS) via dipping the prepared samples on a Cu-net, X-ray

Photoelectron Spectroscopy (XPS) was conducted on XPSESCALAB 250Xi analyser. X-ray diffraction (XRD) parameters were obtained using a Rigaku Ultima IV diffractometer at a rate of 5° $min^{-1}$ from 5° to 80°. The Brunauer-Emmett-Teller (BET) method was utilized to calculate the specific surface area. The adsorption and desorption measurements for $N_2$ were performed on ASAP2460 (Micromeritics) at low temperature of 77 K. Raman spectra were collected on a LabRAM HR Evolution (HORIBA) using a laser with an excitation wavelength of 532 nm. Fourier Transform Infrared Spectroscopy (FTIR) was performed on KBr pellets in the range from 4000 to 400 $cm^{-1}$ using Thermo Nicolet iS5. Thermo-gravimetric analysis (TGA) were recorded using NETZSCH STA 449C analyzer from 25 to 900 °C at a heating rate of 10 °C $min^{-1}$ under the protection of $N_2$.

**Electrochemical Measurements**[1-6]: The electrochemical measurements were carried out using RRDE-3A electrochemical workstation in a general three-electrode system, in which Ag/AgCl (saturated KCl) regarded as the reference electrode, platinum wire (Pt-wire) as the counter electrode, rotating disk electrode (RDE) coated with catalyst as the working electrode, and 0.1 M KOH as the electrolyte. Before each measurement, the solution was purged with high purity Ar or $O_2$ gas for at least 30 minutes to ensure the gas saturation. The catalyst ink was prepared by dispersing 5 mg of catalyst powder with the mixed solvent of water-ethanol-Nafion (v/v/v=2/15/1) by sonication for 30 minutes. The reference Pt/C (20%) cathode was prepared by same method. All the potentials in this work were converted to the reversible hydrogen electrode (RHE) according to the Nernst equation ($E_{RHE}=E_{(Ag/AgCl)}+0.059\times pH+0.197$). For oxygen reduction reaction (ORR), the cyclic voltammetry (CV) tests were performed over voltages ranging from 0.2 to -0.8V (vs. Ag/AgCl) at a scan rate of 50 mV $s^{-1}$ using Ar or $O_2$-saturated 0.1 M KOH electrolyte. For oxygen evolution reaction (OER), CV tests was obtained in the $O_2$-saturated 1 M KOH electrolyte at the potential from 0.9 to 0.3 V (vs. Ag/AgCl) at a scan rate of 10 mV $s^{-1}$. In ORR polarization measurement, linear sweep voltammetry (LSV) using RRDE or RDE were conducted with the electrode rotated from 400 to 2500 rpm, and contrast with the current in Ar-saturated 0.1 M KOH electrolyte. The electron transfer number (n) was calculated according to the Koutecky-Levich Equation:[7]

$$\frac{1}{J}=\frac{1}{J_L}+\frac{1}{J_K}=\frac{1}{B\varpi^{1/2}}+\frac{1}{J_K} \qquad \text{(S1)}$$

-

Where J is the current density, $J_L$ is the current that was measured; $J_K$ represents the kinetic-limiting current and ω is the rotation speeds of electrode.

$$B = 0.62nFC_0(D_0)^{2/3}V^{-1/6} \quad \text{(S2)}$$

In equation S2[8], n is the total number of transferred electrons during the oxygen reduction process; F is Faradaic constant (F = 96485 C $mol^{-1}$), $C_0$ is the $O_2$ concentration (solubility) in 0.1 M KOH electrolyte ($1.2\times10^{-6}$ mol $cm^{-3}$ ); $D_0$ is the $O_2$ diffusion coefficient ($1.90\times10^{-5}$ $cm^2$ $s^{-1}$), and V is the kinematic viscosity of the $O_2$ saturated 0.1 M KOH solution (0.01 $cm^2$ $s^{-1}$).

The LSV for OER were performed from 0.9 to 0.3 V at 1600 rpm in Ar-saturated electrolyte and calibrated by an average of forward and backward currents. To study the catalysts/electrolyte interface, the electrochemical impedance spectroscopy (EIS) was performed in the frequency of 0.01-100 kHz with an AC voltage with 5mV amplitude. The methanol crossover measurements were also recorded by chronoamperometry (i-t) at the half-potential with a rotation speed of 1600 rpm with the addition of 10 mL methanol into 0.1 M KOH electrolyte at around 400 s. The rotating ring disk electrode (RRDE) measurements were performed to calculate the yield of $H_2O_2$ (%) and the electron transfer number (n) based on the equations as follows:

$$H_2O_2(\%) = 200\frac{I_R/N}{I_D + I_R/N} \quad \text{(S3)}$$

$$n = 4\frac{I_D}{I_D + I_R/N} \quad \text{(S4)}$$

In equation S3 and S4, $I_R$ is the ring current, $I_D$ is the disk current, and the collection efficiency of the Pt ring (N=0.4581).[9-10]

**Zn-air battery**

Zn-air battery performance was tested using a home-made liquid Zn-air battery.[11-13] The air-cathodes for primary Zn-air battery were prepared by coating the catalysts (1.5 mg $cm^{-2}$) on a hydrophobic carbon paper, while the polished Zn plate was used as the anode, evaluated in 6 M KOH electrolyte containing 0.2 M $Zn(OAc)_2$. Cycling test was performed using recurrent galvanostatic pulses for 10 min of discharge followed by 10 min of charge at 10 mA $cm^{-2}$ (LAND

CT2001A Model Battery Test System, LANHE Company, Wuhan). The energy density was calculated according to the followed Equation S5: [14]

$$P = I * V \qquad \text{(S5)}$$

Where I represents the discharge current density and V refers to the corresponding voltage. The polarization curves of charge and discharge were performed by the LSV method at a scan rate of 10 mV $s^{-1}$. The specific capacity was determined using the galvanostatic discharge plot and calculated as Equation S6:[15]

$$\text{Specific capacity(mAh g}^{-1}) = \frac{\text{Specific capacity(mAh g}^{-1})}{\text{Weight of consumed Zn}} \qquad \text{(S6)}$$

All battery tests were carried out on LAND CT 2001A multichannel battery testers at room temperature in oxygen atmosphere. All the potentials throughout this paper were referred to the potential of the $Zn/Zn^{2+}$ standard couple.

## Section 2. TGA and XRD

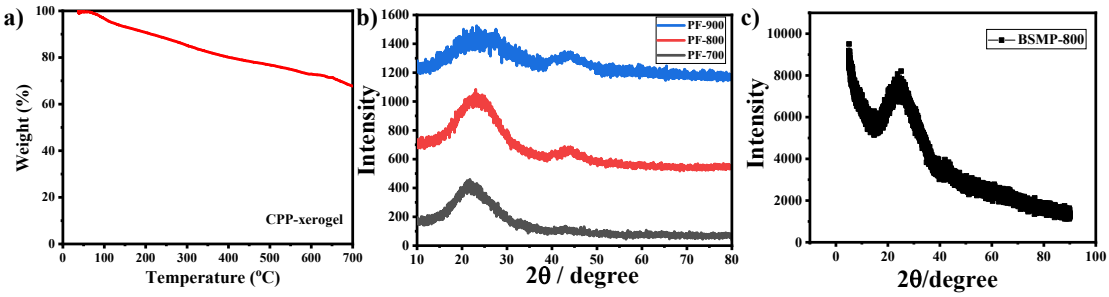


**Figure S1.** a) TG of CPP; b) XRD of PF-X series catalysts; c) XRD of BSMP-800.

## Section 3. X-ray Photoelectron Spectra (XPS)

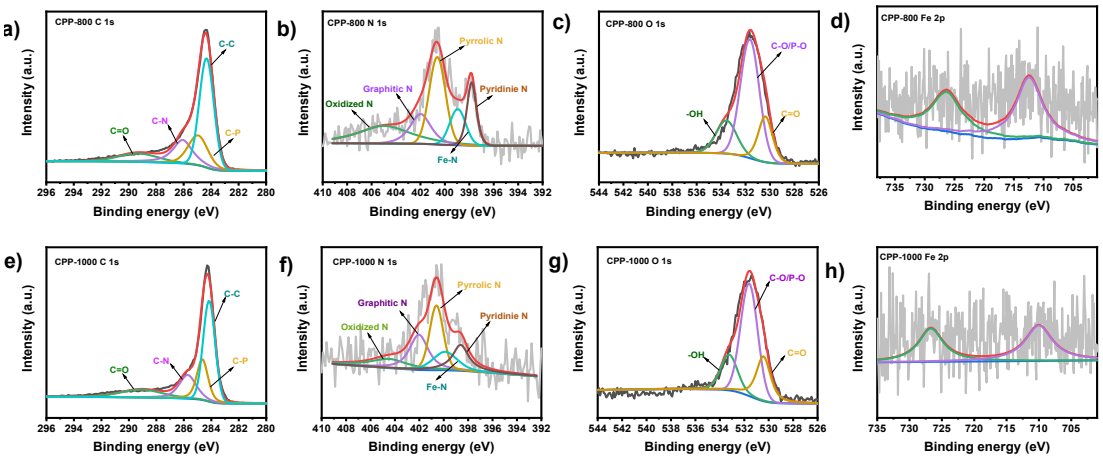


**Figure S2.** a) High-resolution C 1s XPS spectra of CPP-800; b) High-resolution N 1s XPS spectra of CPP-800; c) High-resolution O 1s XPS spectra of CPP-800; d) High-resolution Fe 2p XPS spectra of CPP-800; e) High-resolution C 1s XPS spectra of CPP-1000; f) High-resolution N 1s XPS spectra of CPP-1000; g) High-resolution O 1s XPS spectra of CPP-1000; h) High-resolution Fe 2p XPS spectra of CPP-1000.

## Section 4. EDS

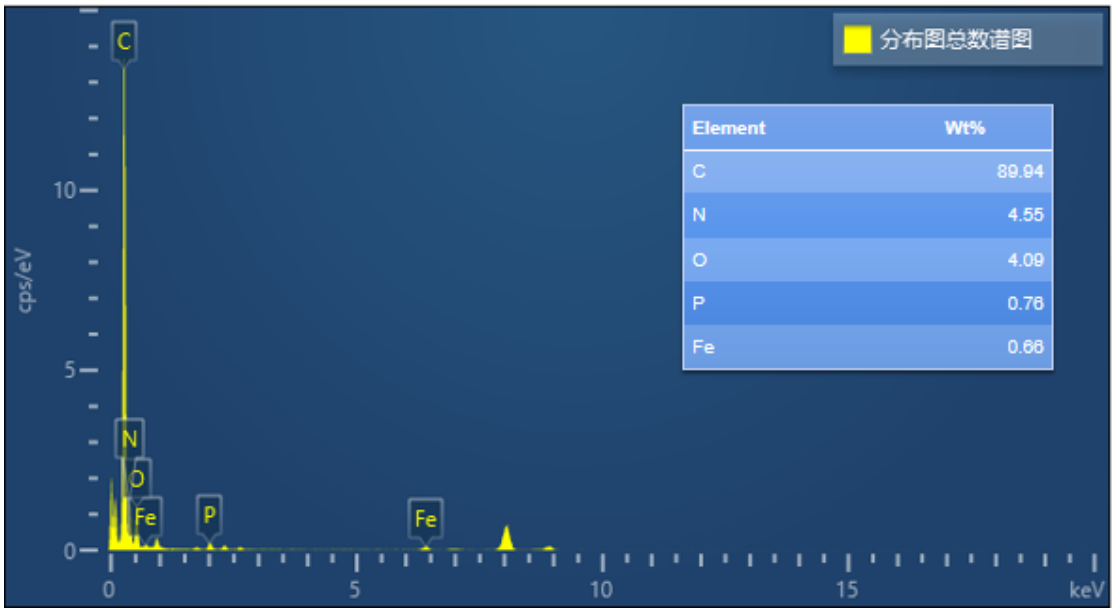


**Figure S3.** EDS of PM-900.

## Section 5. Electrochemical Performance

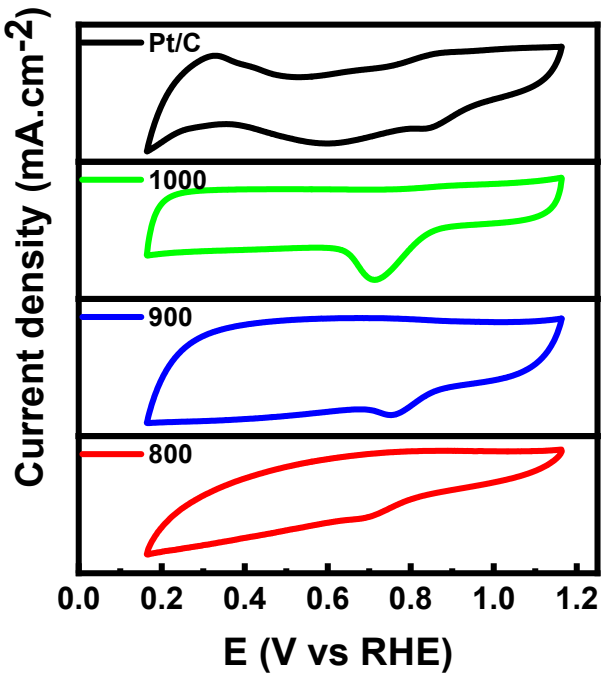


**Figure S4.** CV curves of CPP-900, CPP-800, CPP-1000 and Pt/C in oxygen saturated 0.1 M KOH.

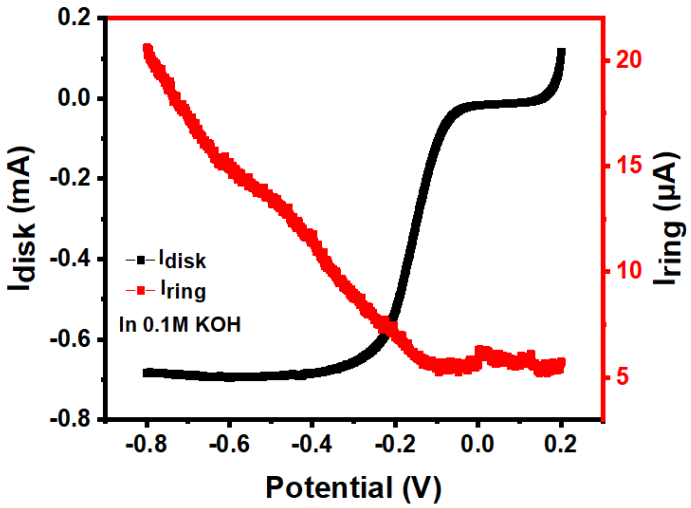


**Figure S5.** $I_{ring}$ and $I_{disk}$ of CPP-900 in 0.1M KOH

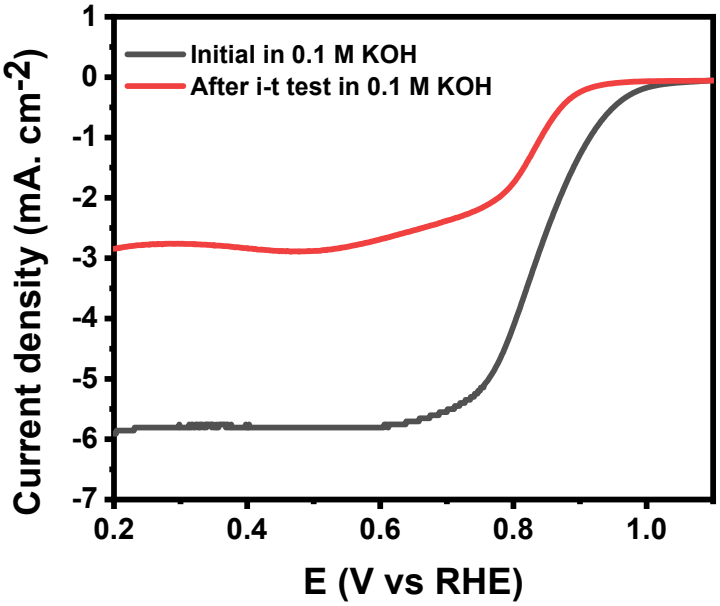


**Figure S6.** LSV curve of Pt/C recorded before and after the i-t test.

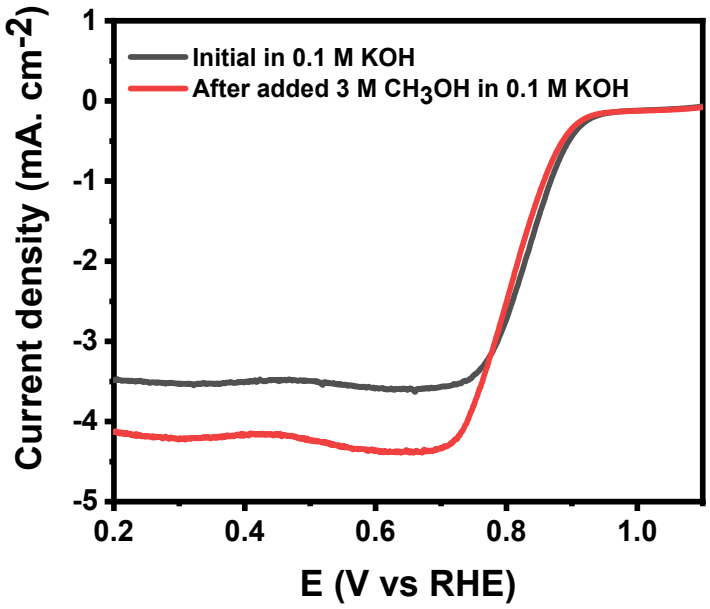


**Figure S7.** LSV curve of CPP-900 recorded before and after the injection of $CH_3OH$ in 0.1 M KOH.

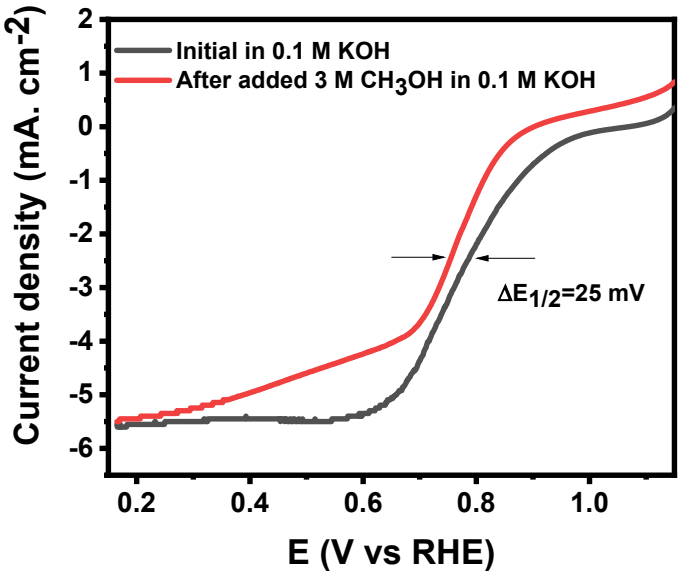


**Figure S8.** LSV curve of Pt/C recorded before and after the injection of $CH_3OH$ in 0.1 M KOH.

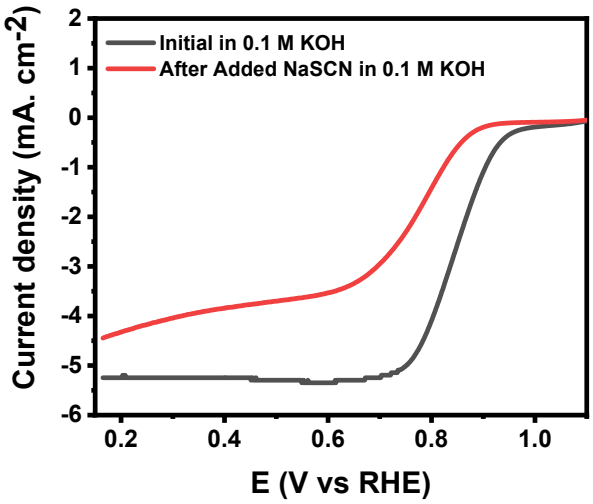


**Figure S9.** LSV curve of CPP-900 recorded before and after the injection of $SCN^{-1}$.

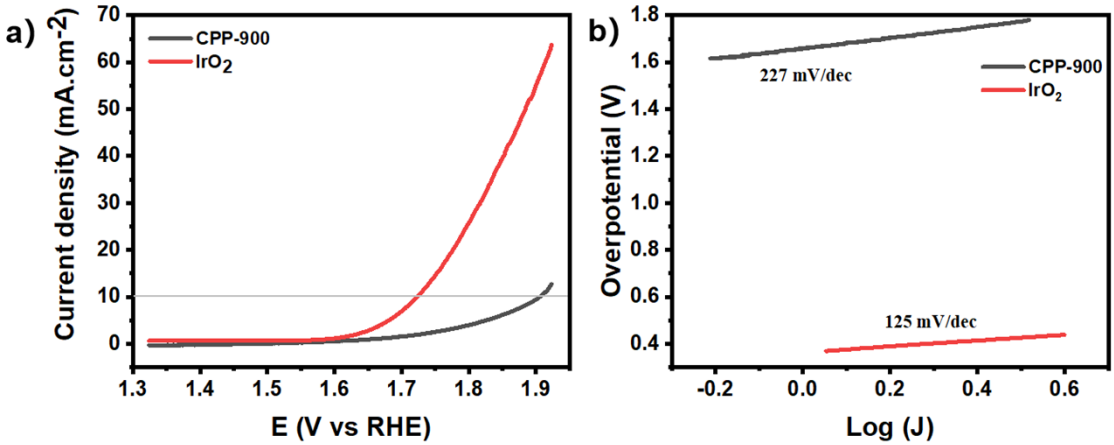


**Figure S10.** a) LSV polarization curves on OER of CPP-900 recorded 1 M KOH at 1600 rpm; b) Tafel plots of CPP-900 and commercial $IrO_2$.

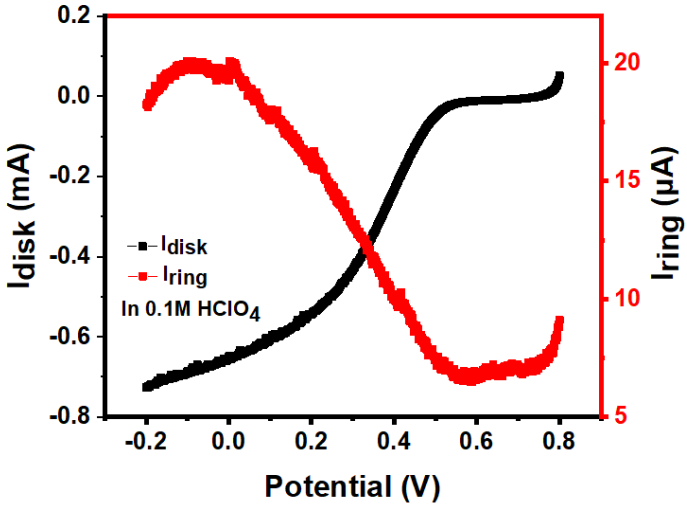


**Figure S11.** $I_{ring}$ and $I_{disk}$ of CPP-900 in 0.1 M $HClO_4$

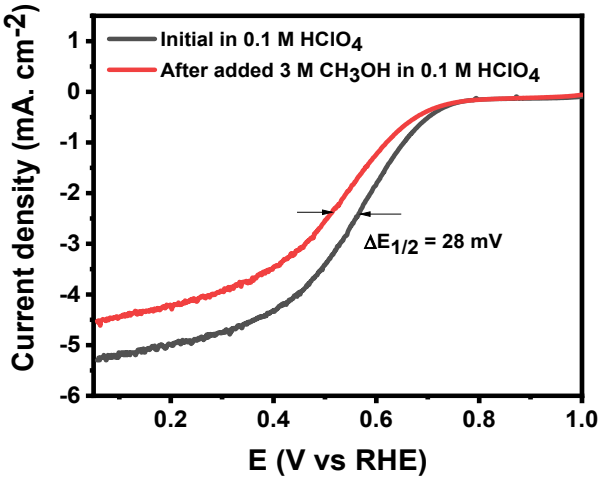


**Figure S12.** LSV curve of CPP-900 recorded before and after the injection of $CH_3OH$ in 0.1 M $HClO_4$.

## Section 6. Supporting Tables

**Table S1. The surface element contents of CPP-X catalysts calculated by the XPS spectra.**

| Sample | C (at%) | O (at%) | N (at%) | Fe (at%) | P (at%) |
|---|---|---|---|---|---|
| CPP-800 | 82.35 | 11.96 | 4.78 | 0.53 | 0.37 |
| CPP-900 | 82.45 | 11.13 | 5.43 | 0.41 | 0.59 |
| CPP-1000 | 88.53 | 8.84 | 2.17 | 0.52 | 0.3 |

**Table S2. Porosity Parameters of prepared polymers and corresponding catalysts**

| Sample | BET ($m^2/g$) | $V_{total}$ ($cm^3/g$) | Average Pore size(nm) |
|---|---|---|---|
| CPP | 57.73 | 0.1963 | 3.54 |
| CPP-800 | 403.1 | 0.417 | 2.77 |
| CPP-900 | 1002.6 | 0.837 | 1.31 |
| CPP-1000 | 319.7 | 0.382 | 2.87 |

**Table S3. The comparison of the electrochemical performance toward ORR among other recently reported electrocatalysts in 0.1 M KOH.**

| Sample | Onset potential ($E_{onset}$, V) | Half-wave potential ($E_{1/2}$,V) | Current density (mA $cm^{-2}$;at 0.5 V) | Ref. |
|---|---|---|---|---|
| **CPP-900** | 0.986 | 0.848 | 5.24 | This work |
| **NCF-900** | 1.05 | 0.89 | 8.66 | [16] |
| **Ni-NC700** | 0.86 | 0.75 | 2.05 | [17] |
| **CP-CMP-900** | 0.997 | 0.85 | 4.78 | [18] |
| **α-$Fe_2O_3$/Fe@NPC** | 1.01 | 0.88 | 5.06 | [19] |
| **FeN@FCS-900** | 0.93 | 0.78 | 4.99 | [20] |
| **PBSCF** | 0.7 | 0.5 | 2.5 | [21] |
| **cal-FeZIF-NSC-0.2** | 0.97 | 0.78 | 5.07 | [22] |

**Table S4. The comparison of the electrochemical performance toward ORR among other recently reported electrocatalysts in 0.1 M $HClO_4$.**

| Sample | Onset potential ($E_{onset}$, V) | Half-wave potential ($E_{1/2}$,V) | Current density (mA $cm^{-2}$;at 0.5 V) | Ref. |
|---|---|---|---|---|
| **CPP-900** | 0.792 | 0.62 | 5.91 | This work |
| **N-FeGly/C** | 0.8 | 0.63 | 4.4 | [23] |
| **[Fe(NCs)]_950** | 0.8 | 0.7 | 4.75 | [24] |
| **Fe-N-C@MXene** | 0.832 | 0.777 | 5.7 | [25] |
| **(Fe,Co)/N-C** | 1.06 | 0.863 | 5.69 | [26] |
| **Fe2P/FeP-PNC** | 0.92 | 0.7 | 5.31 | [27] |
| **Co-Fe SAs/NC** | 0.86 | 0.75 | 6.25 | [28] |
| **Co/Co3O4@C** | 0.782 | 0.672 | 5.32 | [29] |

## Section 8. Supporting References


[1] Y. Kang, W. Wang, J. Li, Y. Mi, H. Gong, Z. Lei, 3D Rosa centifolia-like $CeO_2$ encapsulated with N-doped carbon as an enhanced electrocatalyst for Zn-air batteries, J Colloid Interface Sci, 578 (2020) 796-804.

[2] J. Chen, C. Fan, X. Hu, C. Wang, Z. Huang, G. Fu, J.M. Lee, Y. Tang, Hierarchically Porous Co/Cox My (M = P, N) as an Efficient Mott-Schottky Electrocatalyst for Oxygen Evolution in Rechargeable Zn-Air Batteries, Small, 15 (2019) 1901518.

[3] J. Cai, Q. Zhou, B. Liu, X. Gong, Y. Zhang, K. Goh, D. Gu, L. Zhao, X. Sui, Z. Wang, A sponge-templated sandwich-like cobalt-embedded nitrogen-doped carbon polyhedron/graphene composite as a highly efficient catalyst for Zn-air batteries, Nanoscale, 12 (2020) 973-982.

[4] C. Liu, Z. Wang, X. Zong, Y. Jin, D. Li, Y. Xiong, G. Wu, N & S-co-doped carbon nanofiber network embedded with ultrafine NiCo nanoalloy for efficient oxygen electrocatalysis and Zn-air batteries, Nanoscale, 12 (2020) 9581-9589.

[5] Y. Pan, S. Liu, K. Sun, X. Chen, B. Wang, K. Wu, X. Cao, W.C. Cheong, R. Shen, A. Han, Z. Chen, L. Zheng, J. Luo, Y. Lin, Y. Liu, D. Wang, Q. Peng, Q. Zhang, C. Chen, Y. Li, A

Bimetallic Zn/Fe Polyphthalocyanine-Derived Single-Atom Fe-$N_4$ Catalytic Site:A Superior Trifunctional Catalyst for Overall Water Splitting and Zn-Air Batteries, Angew. Chem. Int. Ed. 57 (2018) 8614-8618.

[6] L. Li, Y. Li, Y. Xiao, R. Zeng, X. Tang, W. Yang, J. Huang, K. Yuan, Y. Chen, $Fe_3O_4$-Encapsulating N-doped porous carbon materials as efficient oxygen reduction reaction electrocatalysts for Zn-air batteries, Chem Commun, 55 (2019) 7538-7541.

[7] J. Gao, J. Wang, L. Zhou, X. Cai, D. Zhan, M. Hou, L. Lai, $Co_2P$@N,P-Codoped Carbon Nanofiber as a Free-Standing Air Electrode for Zn-Air Batteries: Synergy Effects of CoNx Satellite Shells, ACS Appl Mater Interfaces, 11 (2019) 10364-10372.

[8] C. Zhang, F. Kong, Y. Qiao, Q. Zhao, A. Kong, Y. Shan, 3D Graphene-Carbon Nanotube Hybrid Supported Coupled Co-MnO Nanoparticles as Highly Efficient Bifunctional Electrocatalyst for Rechargeable Zn-Air Batteries, Chem Asian J, 15 (2020) 3535-3541.

[9] K. Wang, W. Wu, Z. Tang, L. Li, S. Chen, N.M. Bedford, Hierarchically Structured $Co(OH)_2$/CoPt/N-CN Air Cathodes for Rechargeable Zinc-Air Batteries, ACS Appl Mater Interfaces, 11 (2019) 4983-4994.

[10] Y. Xiao, B. Guo, J. Zhang, C. Hu, R. Ma, D. Wang, J. Wang, A bimetallic MOF@graphene oxide composite as an efficient bifunctional oxygen electrocatalyst for rechargeable Zn-air batteries, Dalton Trans, 49 (2020) 5730-5735.

[11] T.V. Pham, Y. Li, W.B. Luo, H.P. Guo, X.W. Gao, J.Z. Wang, H.K. Liu, Binder-Free 3D Integrated Ni@$Ni_3Pt$ Air Electrode for Zn-Air Batteries, Glob Chall, 3 (2019) 1900027.

[12] L. Ge, D. Wang, P. Yang, H. Xu, L. Xiao, G.X. Zhang, X. Lu, Z. Duan, F. Meng, J. Zhang, M. An, Graphite N-C-P dominated three-dimensional nitrogen and phosphorus Co-doped holey graphene foams as high-efficiency electrocatalysts for Zn-air batteries, Nanoscale, 11 (2019) 17010-17017.

[13] J. Zhao, H. Hu, M. Wu, N-Doped-carbon/cobalt-nanoparticle/N-doped-carbon multi-layer sandwich nanohybrids derived from cobalt MOFs having 3D molecular structures as bifunctional electrocatalysts for on-chip solid-state Zn-air batteries, Nanoscale, 12 (2020) 3750-3762.

[14] P. Yu, L. Wang, F. Sun, Y. Xie, X. Liu, J. Ma, X. Wang, C. Tian, J. Li, H. Fu, Co Nanoislands Rooted on Co-N-C Nanosheets as Efficient Oxygen Electrocatalyst for Zn-Air Batteries, Adv Mater, 31 (2019) 1901666.

[15] Z. Fu, S. Liu, Z. Mai, Z. Tang, D.D. Qin, Y. Tian, X. Wang, Heterostructure and Oxygen Vacancies Promote $NiFe_2O_4/Ni_3S_4$ toward Oxygen Evolution Reaction and Zn-Air Batteries, Chem Asian J, 15 (2020) 3568-3574.

[16] X. Yang, K. Li, D. Cheng, W. Pang, J. Lv, X. Chen, H.-Y. Zang, X. Wu, H. Tan, Y. Wang, Y. Li, Nitrogen-doped porous carbon: highly efficient trifunctional electrocatalyst for oxygen reversible catalysis and nitrogen reduction reaction, Journal of Materials Chemistry A, 6 (2018) 7762-7769.

[17] B. Devi, R.R. Koner, A. Halder, Ni(II)-Dimeric Complex-Derived Nitrogen-Doped Graphitized Carbon-Encapsulated Nickel Nanoparticles: Efficient Trifunctional Electrocatalyst for Oxygen Reduction Reaction, Oxygen Evolution Reaction, and Hydrogen Evolution Reaction, ACS Sustainable Chemistry & Engineering, 7 (2018) 2187-2199.

[18] M. Zhang, J. Ming, W. Zhang, J. Xie, P. Lin, X. Song, X. Chen, X. Wang, B. Zhou, Porous Organic Polymer-Derived $Fe_2P$@N,P-Codoped Porous Carbon as Efficient Electrocatalysts for pH Universal ORR, ACS Omega, 5 (2020) 7225-7234.

[19] Y. Wu, M. Li, L. Ma, M. Lu, H. Zhang, M. Qi, Activating bimetallic ZIF-derived polymers using facile steam-etching for the ORR, New Journal of Chemistry, 46 (2022) 13629-13635.

[20] B. Jiang, S. Wang, F. Meng, L. Ju, W. Jiang, Q. Ji, H.-D. Quan, Enhancing the ORR activity of fullerene-derived carbons by implanting Fe in assembled diamine-$C_{60}$ spheres, CrystEngComm, 24 (2022) 5783-5791.

[21] C. Wang, Z. Zheng, Z. Chen, X. Luo, B. Hou, M. Gholizadeh, X. Gao, X. Fan, Z. Tan, Enhancement on $PrBa_{0.5}Sr_{0.5}Co_{1.5}Fe_{0.5}O_5$ Electrocatalyst Performance in the Application of Zn-Air Battery, Catalysts, 12 (2022) 800.

[22] Y. Li, J. Liu, L. Zheng, Y. Zhang, W. Zhou, K. Shi, H. Xu, J. Gao, Deep-breathing Fe-doped superstructure modified by polyethyleneimine as oxygen reduction electrocatalysts for Zn–air batteries, CrystEngComm, 24 (2022) 5792-5800.

[23] R. Mohan, A. Modak, A. Schechter, Plasma-Modified FeGly/C as a Pt-Free Stable ORR Electrocatalyst in an Acid Electrolyte, ACS Applied Energy Materials, 4 (2021) 564-574.

[24] B. Koyuturk, E.M. Farber, F.E. Wagner, T.-P. Fellinger, D. Eisenberg, A simple decagram-scale synthesis of an atomically dispersed, hierarchically porous Fe–N–C catalyst for acidic ORR, Journal of Materials Chemistry A, (2022). DOI: 10.1039/D2TA00925K.

[25] W. Wang, N. Batool, T. Zhang, J. Liu, X. Han, J. Tian, R. Yang, When MOFs meet MXenes: superior ORR performance in both alkaline and acidic solutions, Journal of Materials Chemistry A, 9 (2021) 3952-3960.

[26] J. Wang, Z. Huang, W. Liu, C. Chang, H. Tang, Z. Li, W. Chen, C. Jia, T. Yao, S. Wei, Y. Wu, Y. Li, Design of N-Coordinated Dual-Metal Sites: A Stable and Active Pt-Free Catalyst for Acidic Oxygen Reduction Reaction, J. Am. Chem. Soc, 139 (2017) 17281-17284.

[27] D. Xue, F. Yu, Q. Ying, Y. Wu, W.J. Lee, S.H. Kwon, Y. Yang, Phosphate-Assisted Dispersion of Iron Phosphide in Carbon Nanosheets towards Efficient and Durable ORR Catalysts in Acidic and Alkaline Media, ChemCatChem, 13 (2021) 4431-4441.

[28] H. Gharibi, N. Dalir, M. Jafari, M. Parnian, M. Zhiani, Engineering dual metal single-atom sites with the nitrogen-coordinated nonprecious catalyst for oxygen reduction reaction (ORR) in acidic electrolyte, Applied Surface Science, 572 (2022) 151367.

[29] Q. Zhang, X. Zhao, X. Miao, W. Yang, C. Wang, Q. Pan, ZIF-L-Co@carbon fiber paper composite derived $Co/Co_3O_4$@C electrocatalyst for ORR in alkali/acidic media and overall seawater splitting, International Journal of Hydrogen Energy, 45 (2020) 33028-33036.